



AFRL-RX-WP-TP-2012-0255

**OXIDATION BEHAVIOR OF A REFRACTORY
NbCrMo_{0.5}Ta_{0.5}TiZr ALLOY (PREPRINT)**

**D.M. Dimiduk, C. Woodward, and D.B. Miracle
Metals Branch
Metals, Ceramics & Nondestructive Evaluation Division**

**O.N. Senkov and S.V. Senkova
UES Inc.**

MARCH 2012

Approved for public release; distribution unlimited.

See additional restrictions described on inside pages

STINFO COPY

**AIR FORCE RESEARCH LABORATORY
MATERIALS AND MANUFACTURING DIRECTORATE
WRIGHT-PATTERSON AIR FORCE BASE, OH 45433-7750
AIR FORCE MATERIEL COMMAND
UNITED STATES AIR FORCE**

NOTICE AND SIGNATURE PAGE

Using Government drawings, specifications, or other data included in this document for any purpose other than Government procurement does not in any way obligate the U.S. Government. The fact that the Government formulated or supplied the drawings, specifications, or other data does not license the holder or any other person or corporation; or convey any rights or permission to manufacture, use, or sell any patented invention that may relate to them.

This report was cleared for public release by the USAF 88th Air Base Wing (88 ABW) Public Affairs Office and is available to the general public, including foreign nationals. Copies may be obtained from the Defense Technical Information Center (DTIC) (<http://www.dtic.mil>).

AFRL-RX-WP-TR-2012-0255 HAS BEEN REVIEWED AND IS APPROVED FOR PUBLICATION IN ACCORDANCE WITH ASSIGNED DISTRIBUTION STATEMENT.

//SIGNED//

ANDREW ROSENBERGER, Program Manager
Metals Branch
Metals, Ceramics & Nondestructive Evaluation Division

//SIGNED//

PAUL RET, Branch Chief
Metals Branch
Metals, Ceramics & Nondestructive Evaluation Division

//SIGNED//

CHARLES H. WARD, Division Chief
Metals, Ceramics & Nondestructive Evaluation Division
Materials and Manufacturing Directorate

This report is published in the interest of scientific and technical information exchange, and its publication does not constitute the Government's approval or disapproval of its ideas or findings.

*Disseminated copies will show “//signature//” stamped or typed above the signature blocks.

REPORT DOCUMENTATION PAGE					Form Approved OMB No. 0704-0188	
<p>The public reporting burden for this collection of information is estimated to average 1 hour per response, including the time for reviewing instructions, searching existing data sources, gathering and maintaining the data needed, and completing and reviewing the collection of information. Send comments regarding this burden estimate or any other aspect of this collection of information, including suggestions for reducing this burden, to Department of Defense, Washington Headquarters Services, Directorate for Information Operations and Reports (0704-0188), 1215 Jefferson Davis Highway, Suite 1204, Arlington, VA 22202-4302. Respondents should be aware that notwithstanding any other provision of law, no person shall be subject to any penalty for failing to comply with a collection of information if it does not display a currently valid OMB control number. PLEASE DO NOT RETURN YOUR FORM TO THE ABOVE ADDRESS.</p>						
1. REPORT DATE (DD-MM-YY) March 2012		2. REPORT TYPE Technical Paper		3. DATES COVERED (From - To) 1 March 2012 – 1 March 2012		
4. TITLE AND SUBTITLE OXIDATION BEHAVIOR OF A REFRACTORY NbCrMo0.5Ta0.5TiZr ALLOY (PREPRINT)				5a. CONTRACT NUMBER In-house		
				5b. GRANT NUMBER		
				5c. PROGRAM ELEMENT NUMBER 62102F		
6. AUTHOR(S) D.M. Dimiduk, C. Woodward, and D.B. Miracle (AFRL/RXLM) O.N. Senkov and S.V. Senkova (UES Inc.)				5d. PROJECT NUMBER 4347		
				5e. TASK NUMBER 20		
				5f. WORK UNIT NUMBER LM121100		
7. PERFORMING ORGANIZATION NAME(S) AND ADDRESS(ES) Metals, Ceramics & Nondestructive Evaluation Division Metals Branch Air Force Research Laboratory, Materials and Manufacturing Directorate Wright-Patterson Air Force Base, OH 45433-7750 Air Force Materiel Command, United States Air Force				8. PERFORMING ORGANIZATION REPORT NUMBER AFRL-RX-WP-TP-2012-0255		
9. SPONSORING/MONITORING AGENCY NAME(S) AND ADDRESS(ES) Air Force Research Laboratory Materials and Manufacturing Directorate Wright-Patterson Air Force Base, OH 45433-7750 Air Force Materiel Command United States Air Force				10. SPONSORING/MONITORING AGENCY ACRONYM(S) AFRL/RXLM		
				11. SPONSORING/MONITORING AGENCY REPORT NUMBER(S) AFRL-RX-WP-TP-2012-0255		
12. DISTRIBUTION/AVAILABILITY STATEMENT Approved for public release; distribution unlimited.						
13. SUPPLEMENTARY NOTES The U.S. Government is joint author of this work and has the right to use, modify, reproduce, release, perform, display, or disclose the work. PA Case Number and clearance date: 88ABW-2012-0779, 15 Feb 2012. Preprint journal article to be submitted to Materials Science and Engineering. This document contains color.						
14. ABSTRACT Isothermal oxidation behavior of a refractory high entropy NbCrMo0.5Ta0.5TiZr alloy was studied during heating at 1273 K for 100 hours in flowing air. Continuous weight gain occurred during oxidation and the time dependence of the weight gain per unit surface area was described by a parabolic dependence with the time exponent $n = 0.6$. X-ray diffraction and scanning electron microscopy (SEM) accompanied by energy dispersive X-ray spectroscopy (EDS) showed that the continuous oxide scale was made of complex oxides and only local (on the submicron levels) redistribution of the alloying elements occurred during oxidation. The alloy has a better combination of mechanical properties and oxidation resistance than commercial Nb alloys and earlier reported developmental Nb-Si-Al-Ti and Nb-Si-Mo alloys.						
15. SUBJECT TERMS Refractory alloy, oxidation, microstructure						
16. SECURITY CLASSIFICATION OF:			17. LIMITATION OF ABSTRACT: SAR	NUMBER OF PAGES 42	19a. NAME OF RESPONSIBLE PERSON (Monitor) Andrew Rosenberger	
a. REPORT Unclassified	b. ABSTRACT Unclassified	c. THIS PAGE Unclassified			19b. TELEPHONE NUMBER (Include Area Code) N/A	

Oxidation Behavior of a Refractory NbCrMo_{0.5}Ta_{0.5}TiZr Alloy

O.N. Senkov,^{1,2,*} S.V. Senkova,^{1,2} D.M. Dimiduk¹, C. Woodward¹ and D.B. Miracle¹

¹ Air Force Research Laboratory, Materials and Manufacturing Directorate, Wright-Patterson Air Force Base, OH 45433, USA

² UES, Inc., Dayton, OH 45432, USA

ABSTRACT

Isothermal oxidation behavior of a refractory high entropy NbCrMo_{0.5}Ta_{0.5}TiZr alloy was studied during heating at 1273 K for 100 hours in flowing air. Continuous weight gain occurred during oxidation and the time dependence of the weight gain per unit surface area was described by a parabolic dependence with the time exponent $n = 0.6$. X-ray diffraction and scanning electron microscopy (SEM) accompanied by energy dispersive X-ray spectroscopy (EDS) showed that the continuous oxide scale was made of complex oxides and only local (on the submicron levels) redistribution of the alloying elements occurred during oxidation. The alloy has a better combination of mechanical properties and oxidation resistance than commercial Nb alloys and earlier reported developmental Nb-Si-Al-Ti and Nb-Si-Mo alloys.

Keywords: Refractory alloy; oxidation; microstructure.

1 INTRODUCTION

Future requirements for high performance turbine engines inevitably include increasing thrust-to-weight ratio and more fuel efficiency. Basic principles of jet propulsion dictate fuel consumption

* Corresponding author. Phone: 937-2551320, e-mail: oleg.senkov@wpafb.af.mil

to be a function of the fuel energy content, engine propulsion, thermal efficiency and engine weight. The generating power of the high-pressure turbine engine improves with an increase in the turbine inlet temperature [1]. The high-pressure turbine blades that see the highest temperatures in the engine are made from Ni-based superalloys, as these alloys have the best combination of required properties, such as creep resistance, temperature capability, environmental resistance, and damage tolerance, among all known alloys. However, operating temperatures are reaching or exceeding the theoretical limits of these materials whose melting temperatures are in the range of 1440-1600 K. Current state-of-the-art solutions to this materials problem require active or passive cooling, which increase parasitic weight and decrease overall engine efficiency. Numerous attempts to progress beyond superalloys by considering alternatives such as ceramics and intermetallics have been largely unsuccessful, because the required balance of properties, especially toughness and resistance to foreign object damage, is difficult to achieve [2]. Thus, new metallic systems with higher melting points and a good balance of structural properties at high temperatures are in high demand.

Refractory alloys such as niobium (Nb) and molybdenum (Mo) are being examined by academic and industrial groups [3,4,5]. High temperature strength and creep resistance are the key properties of refractory alloys, since considerable alloy softening generally occurs at temperatures above $\sim 0.5-0.6T_m$, where T_m is the absolute melting temperature. At the same time, poor room temperature ductility, poor oxidation resistance at temperatures above ~ 900 K, and high density limit the range of applications of these alloys.

Recently, several new refractory alloys with promising mechanical properties in a wide temperature range have been developed [6,7,8,9,10]. A new, so called high entropy alloying (HEA) approach, invented by Yeh et al. [11,12,13], was used to develop these new refractory

alloys, which contain several principal alloying elements at near equiatomic concentrations. These are MoNbTaW, MoNbTaWV [6,7], NbTaHfTiZr [8,9] and NbCrMo_{0.5}Ta_{0.5}TiZr [10]. The high entropy of mixing and similar atomic radii of the alloying elements result in the formation of a single-phase BCC crystal structure in the first three alloys. However, the presence of Cr, having the atomic radius that is much smaller than the atomic radii of other elements in the fourth alloy, causes additional formation of a minor FCC Laves phase [10].

Due to strongly reduced diffusivity of elements in high entropy alloys [7,12,13], improved oxidation resistance may be expected. In fact, heavy alloying of refractory metals with other elements, such as Al, Cr, Ti, Hf, etc, has been shown to be quite effective in obtaining remarkably improved high-temperature oxidation resistance [14,15]. In the present work, we report on the oxidation behavior of a high-entropy refractory alloy NbCrMo_{0.5}Ta_{0.5}TiZr. A detailed analysis of the microstructure, phases and phase compositions in differently oxidized regions provides useful information about the nature and sequence of oxidation of this complex alloy.

2 EXPERIMENTAL PROCEDURES

The NbCrMo_{0.5}Ta_{0.5}TiZr alloy was prepared by vacuum arc melting of the pure elements, as described in [10]. The actual alloy composition determined with the use of inductively-coupled plasma-optical emission spectroscopy (ICP-OES), is given in Table 1. To close porosity in the as-solidified alloy, it was hot isostatically pressed (HIPd) at 1723 K, 207 MN/m² for 3 hour. The crystal structure was identified with the use of a Rigaku X-ray diffractometer, Cu K α radiation, and the 2 Θ range of 5° to 140°, and using the electron back-scatter diffraction (EBSD) technique. The density of the alloy was measured with an AccuPyc 1330 V1.03 helium

pycnometer. The microstructure and chemical composition of phases were analyzed with the use of a scanning electron microscope (SEM) equipped with a backscatter electron (BSE), energy-dispersive X-ray spectroscopy (EDS), and electron backscatter diffraction (EBSD) detectors. A step size of 0.2 μm was used for simultaneous EDS and EBSD mapping.

Oxidation behavior of the alloy was studied using a TherMax 700 TGA unit (Cahn Instruments, Madison, WI). The initial sample dimensions were 4.69 x 4.68 x 7.66 mm^3 and the sample weight was 1.3814 g. The sample in an alumina crucible was placed in a vertical furnace, heated to the temperature of 1273 K at the rate of 15 K/min, held at 1273 K for 100 hours and furnace cooled (approximately 5-10°C/min). During the whole experiment, dry air flowed continuously through the furnace at a rate of 80 ml/min. The weight of the sample was automatically registered every 20 seconds.

3 RESULTS

3.1 Microstructure of HIPd Alloy

Figure 1 shows the X-ray diffraction pattern of the HIPd NbCrMo_{0.5}Ta_{0.5}TiZr alloy. A major BCC1 phase and two minor phases, BCC2 and FCC (Laves), were identified [10]. The lattice parameters of these phases were determined to be $a = 324.76 \pm 0.16$ pm, 341 ± 1 pm and 740.0 ± 0.5 pm, respectively.

Microstructure of the HIPd alloy is shown in Figure 2. Three characteristic constituents are clearly recognized on the backscatter electron (BSE) images. These are (i) large branching bright particles, (ii) a dark continuous matrix between the bright particles, and (iii) smaller dark particles precipitated inside the matrix. EBSD analysis indicated that both the bright particles and the dark matrix have the BCC crystal structures, whereas the dark particles have a FCC crystal

structure (Figure 3a, b). (Note that in the secondary electron (SE) image mode, Figure 3a, the gray color code of the FCC particles is similar to the color code of large bright particles.) Although the EBSD method cannot distinguish the BCC1 and BCC2 phases, which have different lattice parameters, these phases can be identified by knowing their volume fractions. Indeed, the volume fractions of the light particles, dark particles and the matrix were determined to be ~67%, 17% and 16%, respectively. Comparing these results with the results of X-ray diffraction, one may conclude that the light particles have the BCC1 crystal structure, while the matrix phase has the BCC2 crystal structure. The BCC1 particles have the same crystallographic orientation as the adjacent BCC2 matrix (Figure 3c,e), while the FCC phase particles are randomly oriented and many of them are twinned (Figure 3d,e). EDS mapping showed that these phases have different concentrations of alloying elements (Figure 4). In particular, the concentration of Ti is much higher in the BCC2 phase than in the BCC1 phase, while the FCC phase has the lowest concentration of Ti (Figure 4a). The concentration of Ta is the highest in the BCC1 phase (Figure 4b) and Cr is mainly located in the FCC phase (Figure 4a). Quantitative chemical analysis of these three phases was conducted with the use of an EDS detector. The results, given in Table 2, indicate that the BCC1 phase was slightly enriched with Nb, Mo and Ta, and depleted with Zr and Cr. The amount of Ti in the BCC1 phase is close to the average alloy composition. The BCC2 phase, on the other hand, was highly enriched with Zr and Ti and depleted with Mo, Cr and Ta. The amount of Nb in this phase was only slightly lower of the average alloy composition. Finally, the FCC phase contained an increased amount of Cr (~41 at.%) and reduced amounts of Mo, Nb, Ta and Ti.

3.2 Oxidation Behavior at 1273 K

Continuous weight gain occurred during holding the NbCrMo_{0.5}Ta_{0.5}TiZr alloy sample at 1273 K in air (Figure 5). The initial sample dimensions were 4.69 x 4.68 x 7.66 mm³ and the sample weight was 1381.4 mg. At the time when the furnace reached 1273 K and the oxidation experiment started, the sample weight was 1397.1 mg. The weight of the sample rapidly increased during first 10 hours of holding at 1273 K, but the rate of the weight increase continuously decreased with an increase in the oxidation time (Figure 5). Such behavior can be described by a power-law dependence:

$$\Delta m = k_1 t^n \quad (3)$$

Here Δm is the weight gain per unit surface area, t is the holding time (in seconds) at 1273 K, n is the time exponent and k_1 is the rate constant. The best fit to the experimental data occurs at $n = 0.6$ and $k_1 = 0.055 \text{ mg} \cdot \text{cm}^{-2} \cdot \text{s}^{-0.6}$ (a dashed line in Figure 5).

At the end of the experiment, after 3.6×10^5 seconds (100 h) holding at 1273 K, the weight of the sample was 1620.7 mg. During cooling after the high-temperature exposure, the oxide layer separated from the sample surface, likely due to different coefficients of thermal expansion of the oxide and the alloy. Six plate-like solid pieces of the oxide layer, corresponding to 6 rectangular surfaces of the sample, plus the remaining sample core were collected (Figure 6). The thicknesses of these oxide pieces were approximately the same, ~ 1.75 mm, their total weight was 1016.8 mg and the volume measured by a helium pycnometer was $202.5 \pm 18.2 \text{ mm}^3$. From this data, the average oxide layer density was estimated to be $\rho_{\text{oxide}} = 5.06 \pm 0.46 \text{ g/cm}^3$. The remaining core dimensions were approximately $3.4 \times 3.4 \times 6.4 \text{ mm}^3$ at the core weight of 593.8 mg. The total weight of the recovered sample (1610.6 mg) was 10.1 mg less than the final

weight of the oxidized sample measured at 1273 K. It is quite likely that few small pieces of material were left undetectable in the furnace chamber.

X-ray diffraction of the oxide layer formed on the surface of the NbCrMo_{0.5}Ta_{0.5}TiZr alloy sample during holding at 1000°C for 100 hours showed that this layer consists of many oxides (Figure 7). Several identified oxides are Cr₂O₃, CrNbO₄, Cr₂TiO₅, Cr₂Ti₅O₁₃, CrTaO₄, MoTiTa₈O₂₅, Nb₂O₅, Nb₃Cr₂O₁₀, Nb₂Zr₈O₂₁, Ti₂ZrO₆, Ta₄O₅, and Ta₁₂MoO₃₃ (see Figure 7). Other complex oxides can also be present.

3.3 Microstructure of the Oxidized Layer

Figure 8 shows macro-SEM/BSE images of polished cross-sections of a core (non-oxidized) part (squared shape) and a separated oxide layer of a NbCrMo_{0.5}Ta_{0.5}TiZr alloy sample after the oxidation experiment. The microstructures in the oxide layer and in the core piece look similar; however, the microstructural constituents look larger in the oxide layer, probably due to overall expansion of the oxidized part. Higher magnification images of the oxide layer are shown in Figure 9. The microstructure of the oxide layer repeats the microstructure of the non-oxidized alloy. In accord to the Z-contrast method, no noticeable redistribution of the alloying elements seems to occur. Cracks oriented almost parallel to the sample surface develop in the regions of former BCC2 and Laves phases (between former BCC1 particles). The cracks are also extended into the BCC1 particles, however in much smaller fraction, indicating that the BCC1 phase is more resistant to cracking during oxidation than the two other phases. Another plausible explanation is that the volume expansion of the BCC1 phase is larger than the expansion of other phases during oxidation. This would impose tensile strains on the remaining phases and hence their cracking.

Figure 10 shows high-magnification BSE and SE images of a former BCC1 particle after oxidation. The images were taken at a 30,000x magnification. Different Z contrasts on the BSE image indicate that redistribution of the alloying elements occurred at a scale of less than 0.5 μm and at least three phases are present in the BCC1 particles after oxidation. These are (i) dominated gray regions, (ii) dark regions and (iii) white elongated fine particles. The dark regions are likely to be more enriched with oxygen than the grey and light regions. Fine porosity is also present, mainly inside the dark regions. Similar phase separations are observed inside former BCC2 and FCC phases, supporting the X-ray diffraction results on the formation of many different oxides during oxidation.

The EDS analysis of the former BCC1, BCC2 and FCC phases inside the oxide layer showed about 50 at.% oxygen and noticeable variations of other elements, especially inside BCC2 and FCC phases (Table 3). To compare the compositions of oxide phases with the compositions of the respective non-oxidized phases, oxygen was excluded from counting, and the effective concentrations of the alloying elements in the oxidized phases are given in Table 4. The comparison of the phase compositions before (Table 2) and after (Table 4) oxidation gives the following information. (i) Oxidation considerably reduces the amount of Mo in all three constituents and especially in the BCC1 phase. It is likely that Mo formed volatile oxides which evaporated during oxidation. The presence of fine pores in the former BCC1 phase, which had high concentration (14.3%) of Mo before oxidation, seems to support this suggestion. (ii) The concentrations of Zr, Nb, Ti and Cr in the BCC1 phase increase proportionally to a decrease in Mo, which indicates that these four elements do not escape the BCC1 phase. (iii) A very slight (0.2%) decrease in Ta in the former BCC1 phase is an indication that the effective concentration of Ta, relative to four other elements is reduced in the BCC1 phase. At the same time the

concentration of Ta increases noticeably in the BCC2 phase after oxidation. It is likely that redistribution of Ta between these two BCC phases occurred during oxidation. (iv) The effective concentrations of Zr and Ti decrease and Cr increase in the former BCC2 phase, but the opposite trend for these elements and almost to the same amounts is observed in the former FCC phase, after oxidation. This may indicate that redistribution of these elements between BCC2 and FCC phases occurred at 1273K, which is fixed by the oxidation event.

3.4 Microstructure of the Core Part

The secondary and backscatter electron images of the microstructure of the under-surface region of the core part of the oxidized sample are shown in Figure 11a and Figure 11b, respectively.

Two layers above the non-oxidized matrix are clearly identified. These are (i) a remaining (non-split), ~5 to 80 μm thick, complex oxide layer and (ii) a transition, ~120-160 μm thick, partially oxidized layer. The microstructure and chemistry of the complex oxide layer are similar to those described in Section 3.3. The microstructure and chemistry of the transition layer are different and thus can provide additional information on kinetics of oxidation.

A representative microstructure of the transition layer under the oxide scale is shown in Figure 12 and chemical compositions of different regions, identified in Figure 12, are given in Table 5. Locations of former BCC1 (regions 1 and 2 in Figure 12), BCC2 (regions 3 and 4) and Laves phases (region 5) are clearly distinguished. During oxidation, the BCC2 phase transforms into a lamellar structure consisting of at least two components: dark oxide phase with an increased Zr content and a bright, less oxidized phase, which has the chemistry of the BCC1 phase. Oxidation of the Laves phase (gray particles, similar to region 5 in Figure 12) leads to formation of sharp cracks which seem to cut the particles along specific crystallographic directions. Oxidation of the

Laves phase particles occur evenly and no visible phase separation is seen inside these particles. The surface layer of former BCC1 particles (region 2) becomes darker and small radial cracks form at this layer due to enrichment with oxygen. This analysis indicates that, among three phases presented in the alloy, the BCC1 phase is the most resistant and the BCC2 phase is the least resistant to oxidation. Oxidation of the Laves phase leads to cracking, while oxidation of the BCC2 phase initiates eutectic reaction with the formation of at least two oxide phases. The microstructure of the central region of the core part is given in Figure 13. No oxygen is present in this region and the chemical compositions of the BCC2 and FCC phases are similar to the non-oxidized alloy. Fine precipitates are formed inside the primary BCC1 particles. The EBSD analysis indicates that these precipitates have the FCC structure and are likely the Laves phase [10].

Oxygen distribution inside the core part along the horizontal line shown in Figure 8 is given in Figure 14 (solid dark line). The negative distance values at the horizontal axis correspond to mount material (plastic) and the positive values correspond to the distance from the sample surface. The oxygen concentration is maximum at the sample surface, it exponentially decreases with an increase in the distance from the surface inside the sample, and is zero at the distances of ~150 μm and above. This concentration profile can be described as a sum of two Gaussian distributions, $C_O = A\exp[-(x/\sigma)^2/2]$, where x is the distance from the sample surface and σ is the standard deviation. For the first Gaussian (Gauss1 in Figure 14), $\sigma_1 = 10 \mu\text{m}$, and for the second Gaussian (Gauss2), $\sigma_2 = 50 \mu\text{m}$. Two Gaussian distributions can be due to different diffusivity of oxygen inside the BCC1 particles and in the BCC2 matrix (and in the Laves phase). Taking into account that $\sigma^2 = 2Dt$, where D is the coefficient of diffusion and t is time, one can conclude that the diffusion of oxygen in the BCC1 phase is ~25 times slower than in the BCC2/Laves phases.

4 DISCUSSION

4.1 Oxidation Kinetics

There are two extreme conditions for the oxidation reaction of metallic alloys [16,17,18]. The first condition occurs when oxygen is in direct contact with the surface and the rate-controlling mechanism for the oxidation reaction is a gas-metal interface reaction. In this case the mass gain per unit surface area increases linearly with the oxidation time and the time exponent, n , in Equation (3) is equal to unity ($n = 1$). Oxidation by this mechanism generally occurs when the surface oxide is unable to form a continuous passive layer and retard further oxidation of the substrate alloy due to different reasons such as (a) a smaller oxide volume than the volume of the alloy from which it forms, (b) low vapor pressure and easy evaporation of oxide products, (c) instability of the oxide due to high oxygen solubility and high oxygen transport rates in the matrix, and/or (d) continuous spallation.

The second extreme condition occurs when a crack-free stable surface oxide film forms, which protects the alloy from direct contact with gaseous oxygen, and diffusion through the oxide layer becomes the rate-controlling process for the oxidation reaction. In this case, the oxidation rate (i.e. the rate of the mass gain per unit surface area) decreases with time, and $n = 0.5$. This situation takes place when the volume of the forming surface oxide is the same or larger than the volume of the alloy participating in the reaction and the oxide is well adhered to the matrix [18,19].

During oxidation in continuously flowing air at 1273 K, the new refractory alloy NbCrMo_{0.5}Ta_{0.5}TiZr showed a near-parabolic dependence of the mass gain per unit surface area on the oxidation time, with an overall time exponent $n = 0.6$ (see Figure 5). This value of n is

close to $n = 0.5$ indicating diffusion controlling formation of a protective oxide layer. Indeed, naked eye and mass balance examination, as well as the microstructure analysis, of the oxidized sample revealed formation of a rather solid and dense oxide layer with no radially directed cracks and no oxide spallation during the oxidation process. When the dependence of the mass gain per unit surface area on the oxidation time is plotted in the logarithmic coordinates, two distinct behaviors can clearly be seen (Figure 15). During the first 1500 seconds (~25 minutes) oxidation is fast and $n = 0.85$. In the time range from ~1500 s to 3600 s (25 to 60 minutes) the oxidation rate decreases, n decreases to $n = 0.5$ and keeps this value until the end of the experiment. This analysis indicates that (a) during the first 25 minutes the alloy oxidation is controlled mainly by the oxygen-alloy interface reaction process, (b) within the first 60 minutes the alloy surface is completely covered by a stable oxide film and (c) further oxidation is controlled by the oxygen diffusion through this oxide film.

The density of the oxide, $\rho_{\text{oxide}} = 5.06 \pm 0.46 \text{ g/cm}^3$, is about 38.5% smaller than the density of the alloy, $\rho_{\text{alloy}} = 8.23 \pm 0.01 \text{ g/cm}^3$ [10], which is associated with considerable volume expansion during oxidation. Indeed, assuming that the core (under the oxide layer) part of the sample does not change volume during oxidation, the initial volume of the surface layer, which transformed to the oxide, is estimated to be $V_{\text{SL}} = 94.3 \text{ mm}^3$. After oxidation, this layer expanded to $V_{\text{SO}} = 202.5 \text{ mm}^3$, i.e. more than 2 times.

By knowing the mass of the oxidized surface layer before ($=\rho_{\text{alloy}} \times V_{\text{SL}} = 0.7763 \text{ g}$) and after (1.0168 g) oxidation and the molar weights of the alloy (87.09 g/mol) and oxygen (16.0 g/mol), molar fractions of the metal atoms (i.e. alloying elements, Me) and oxygen (O) in the oxide layer can be estimated. Indeed, the amounts of metal and oxygen atoms in the oxide layer are estimated to be $N_{\text{Me}} = 0.0089 \text{ moles}$ and $N_{\text{O}} = 0.015 \text{ moles}$, respectively, which gives the mole

fractions of metals and oxygen of ~0.37 and 0.63. These fractions are close to the oxide formula Me_3O_5 , which can be considered as a mixture of MeO , MeO_2 and Me_2O_3 oxides ($2\text{Me}_3\text{O}_5 = \text{MeO} + 3\text{MeO}_2 + \text{Me}_2\text{O}_3$).

The above estimations do not take into account that most of molybdenum escape during oxidation due to formation of volatile oxides. If molybdenum is excluded, then the mass of remaining metal elements is reduced from 0.7763 g to 0.6909 g and the molar weight of these elements becomes equal to 86.1 g/mol. The refined mole fractions of metal atoms and oxygen in the oxide layer are 0.286 and 0.714, respectively.

The estimations of the amount of oxygen in the oxide layer (63-71 at.%) conducted in the above two paragraphs are noticeably higher than ~50 at.% determined experimentally by EDS. This discrepancy should indicate that the weight gain was due to not only the reaction with oxygen but also because of nitrogen pickup (nitrating). Unfortunately, nitrogen was not within the list of the elements analyzed by EDS, because its $\text{K}\alpha$ line was shielded by the $\text{L}\alpha$ line from Ti.

4.2 Comparison with Conventional and Developmental Refractory Alloys

The major problem with conventional Mo alloys is low melting points and volatile behavior of molybdenum oxides, which lead to a rapid loss in weight and catastrophic failure at temperatures above ~ 873 K [20,21]. New developmental Mo alloys based on molybdenum silicides and containing boron show considerably improved oxidation resistance at temperatures above 1273K; however, oxidation is still accompanied by weight loss and substantial weight loss still occurs during air exposure at lower temperatures [21,22].

Nb based conventional refractory alloys have extremely poor oxidation resistance at elevated temperatures due to high oxygen solubility and diffusivity in the Nb matrix and protective

coatings are absolutely necessary for these alloys [23,24,25,26]. Without protective coating, oxidation of these alloys occurs very rapidly, with considerable weight gain, which generally exceeds $0.04 \text{ mg/cm}^2/\text{s}$ ($150 \text{ mg/cm}^2/\text{h}$), followed by alloy embrittlement and disintegration. Several developmental Nb alloys with improved oxidation resistance, containing Ti, Si, Al and some other elements, have recently been reported [27,28,29]. Unfortunately, these developmental alloys contain high volume fractions of silicides and aluminides and are brittle at temperatures below $\sim 1000 \text{ K}$. The results of isothermal oxidation at 1273 K of these developmental alloys are given in Table 6. The oxidation data for pure Nb and our NbCrMo_{0.5}Ta_{0.5}TiZr alloy are also given there. Comparison of the data given in Table 6 indicates that the oxidation resistance of the NbCrMo_{0.5}Ta_{0.5}TiZr alloy is much better than that of the Nb-Al, Nb-Si, Nb-Si-Al and Nb-Si-Al-Ti alloys, as well as Nb-13Si-4Mo and Nb-19Si-5Mo alloys, and similar to that of the Nb-18Si-26Mo alloy. However, oxidation resistance of the developmental Nb-12Si-15Mo alloy [29] is slightly better than that of our alloy.

4.3 Oxidation reactions

Oxidation of the high entropy refractory NbCrMo_{0.5}Ta_{0.5}TiZr alloy is accompanied by only limited diffusion of the alloying elements and leads to formation of complex oxides. No element separation and/or preferable metal oxide formation occur during oxidation. The diffusion distances of the alloying elements are estimated to be less than 500 nm , so that morphologies and compositions of the former BCC1, BCC2 and Laves phases retain while oxidation of these phases is accompanied by large volume expansion. This behavior is somewhat different from the oxidation behavior of conventional Nb alloys, as well as developmental Nb-Si-Al-Ti alloys, where a preferable metal oxide scale forms resulting in a decrease in the concentration of the

alloying elements inside the Nb matrix, an increase in the oxygen solubility and eventually internal oxidation [14,28]. Reduced diffusion rates of the alloying elements in high entropy alloys was noted in previous publications [6,12,13] and it was attributed to a reduced concentration of free vacancies in these multi-principal-element alloys. One may therefore conclude that the restricted diffusion of the alloying elements may contribute to formation of many complex oxides in the NbCrMo_{0.5}Ta_{0.5}TiZr alloy. It is also likely that the large number of complex oxides results from the high concentrations of many elements, each of which is a strong oxide former. Due to heavy alloying, low solubility and slow diffusion of oxygen in the alloy is also expected. Indeed, no oxygen was detected in the core part of the oxidized sample at the distances of ~150 μm or higher from the oxide-matrix interface. The effective diffusivity of oxygen in the oxidized alloy can be estimated by taking into account that holding at 1273K for 100 hours results in the complete oxidation of ~0.65mm-thick layer and partial oxidation of the 0.15 mm thick transition layer. This gives the effective coefficient for oxygen diffusion through the oxide/alloy at 1273 K, $D_{\text{O}} \approx 3.0 \times 10^{-9} \text{ cm}^2/\text{s}$. This is two orders of magnitude lower than the oxygen diffusion in pure Nb [30,31].

5 CONCLUSIONS

Oxidation behavior of a refractory NbCrMo_{0.5}Ta_{0.5}TiZr alloy during heating at 1273 K for 100 hours in flowing air was studied. Before oxidation, the alloy consisted of three phases, BCC1, BCC2 and FCC (Laves). The volume fractions of these phases were ~67%, 16% and 17%, respectively. The BCC1 and Laves phases were presented in the form of particles embedded in the continuous BCC2 phase. The BCC1 phase was enriched with Mo, Nb and Ta, the BCC2 phase was enriched with Zr and Ti, and the FCC Laves phase was enriched with Cr and Zr.

The rate of weight gain per unit surface area during oxidation at 1273 K followed a near-parabolic dependence, $\Delta m = k_1 t^n$, with $n = 0.6$ and $k_1 = 7.5 \text{ mg}\cdot\text{cm}^{-2}\cdot\text{h}^{-n}$. This is an indication of formation of protective oxide scale on the sample surface. After 100 h holding at 100 h, the thickness of the oxide scale was $\sim 1.75 \text{ mm}$.

During cooling from 1273 K to room temperature, separation of the oxide layer from the non-oxidized core part of the sample occurred. X-ray diffraction of the separated layer showed that it consisted of many complex oxides. Microstructural and EDS analysis of the oxide layer revealed redistribution of the alloying elements at a scale level of less than 500 nm, indicating slow diffusion of these elements during oxidation. Evaporation of volatile molybdenum oxide decreased the concentration of Mo in the oxide layer and formed microporosity. Cracks oriented almost parallel to the sample surface developed in the regions of the former BCC2 and Laves phases. The cracks were also extended into the former BCC1 particles, however in much smaller fraction, indicating that the BCC1 phase was more resistant to cracking during oxidation than the two other phases.

An about 150 μm thick partially oxidized transition layer was observed under the oxide layer. In this region, oxygen concentration rapidly decreased from the concentration typical to the oxide layer to zero. This concentration profile was described as a sum of two Gaussian distributions,

$$C_o = A \exp\left[-\frac{x^2}{2Dt}\right], \text{ where } x \text{ is the distance from the oxide-layer/matrix interface toward the}$$

sample center, $2A$ is the oxygen concentration at the interface and $Dt = 100 \mu\text{m}$ and $2500 \mu\text{m}$ for the first and second distributions, respectively. Such behavior was explained by slower oxygen diffusion in the BCC1 phase than in two other phases.

6 ACKNOWLEDGEMENTS

Technical support from Drs. Carmen Carney and Fred Meisenkothen is greatly appreciated. This work was supported through the Air Force Research Laboratory Director's Fund and through USAF contract No. FA8650-10-5226.

TABLES

Table 1. Chemical composition of the NbCrMo_{0.5}Ta_{0.5}TiZr alloy produced by vacuum arc melting.

Composition	Zr	Nb	Mo	Ti	Cr	Ta
At. %	18.48	21.84	10.04	19.40	18.39	11.86
Wt. %	19.36	23.30	11.06	10.67	10.98	24.64

Table 2. Chemical composition (in at.%) of the BCC1, BCC2 and FCC phases in the HIPd NbCrMo_{0.5}Ta_{0.5}TiZr alloy.

Phase\Element	Zr	Nb	Mo	Ti	Cr	Ta
BCC1	9.82	26.80	14.30	19.07	13.22	16.80
BCC2	40.60	18.68	0.64	33.16	3.09	3.83
FCC	23.09	12.07	6.35	10.78	40.74	6.99

Table 3. Chemical composition (in at.%) of the former BCC1, BCC2 and FCC phases in oxide layer.

Phase\Element	O	Zr	Nb	Mo	Ti	Cr	Ta
Former BCC1	51.9±1.2	5.5±1.0	14.1±1.0	2.8±0.6	10.3±0.2	7.2±0.5	8.2±0.4
Former BCC2	50.6±1.2	17.6±3.0	9.7±1.5	0.0	14.5±2.0	4.4±1.2	3.3±0.5
Former FCC	48.8±1.2	13.5±2.7	8.1±1.5	1.3±1.3	7.1±1.5	17.4±7.0	3.9±0.8

Table 4. Effective concentrations of the alloying elements (in at.%) in the former BCC1, BCC2 and FCC phases in the oxide layer, without counting oxygen.

Phase\Element	O	Zr	Nb	Mo	Ti	Cr	Ta
Former BCC1	-	11.4±2.0	29.3±2.0	5.9±1.2	21.5±0.4	14.9±1.0	17.0±0.8
Former BCC2	-	35.6±6.0	19.6±3.0	0.0	29.3±4.0	8.8±2.4	6.6±1.0
Former FCC	-	26.3±5.4	15.8±3.0	2.6±2.6	13.8±2.9	33.9±13.6	7.6±1.6

Table 5. Chemical composition (in at.%) of different regions (shown in Figure 12) in the transition (partially oxidized) layer. Effective concentrations of main alloying elements, without counting oxygen, are given in brackets. The numbers in the first column correspond to the respective outlined regions in Figure 12.

Phase\Element	O	Zr	Nb	Mo	Ti	Cr	Ta
1. Former BCC1, center	8.84 (0.00)	15.0 (16.5)	17.5 (19.2)	7.75 (8.50)	20.0 (21.9)	18.2 (20.0)	12.7 (13.9)
2. Former BCC1, surface layer	18.5 (0.00)	9.77 (12.0)	20.7 (25.4)	12.0 (14.7)	15.5 (19.0)	10.6 (13.1)	13.0 (15.9)
3. Former BCC2 (dark)	38.6 (0.00)	36.7 (59.8)	7.37 (12.0)	0.56 (0.91)	7.71 (12.6)	7.26 (11.8)	1.78 (2.90)
4. Former BCC2 (eutectic)	37.0 (0.00)	24.3 (38.6)	11.4 (18.1)	0.53 (0.84)	22.9 (36.4)	1.70 (2.70)	2.16 (3.43)
5. Former FCC	22.7 (0.00)	18.0 (23.2)	9.16 (11.9)	5.52 (7.14)	7.12 (9.21)	32.0 (41.5)	5.51 (7.13)

Table 6. Weight gain per unit surface area (in mg/cm^2) of Nb and several Nb-based developmental alloys during isothermal holding at 1273K in air.

Alloy\Time	1 h	2 h	4 h	24 h	100 h	Ref
Nb	159	300	-	-	-	[29]
Nb-10Si	37	-	-	-	-	[29]
Nb-10.1Si	45	90	170	-	-	[28]
Nb-17.3Al	23	43	65	-	-	[28]
Nb-5Si-9Al	90	160	275	-	-	[28]
Nb-7Si-9Al	69	145	275	-	-	[28]
Nb-8Si-9Al-10Ti	-	-	-	182	338	[28]
Nb-10Si-9Al-10Ti	-	-	-	95	291	[28]
Nb-6Si-11Al-15Ti	-	-	-	51	167	[28]
Nb-8Si-11Al-15Ti	-	-	-	51	153	[28]
Nb-19Si-5Mo	26	53	106	-	-	[29]
Nb-18Si-26Mo	9.7	13.8	19.5	45	-	[29]
Nb-13Si-4Mo	48	105	166	-	-	[29]
Nb-12Si-15Mo	1.3	1.4	4.0	15	-	[29]
NbCrMo0.5Ta0.5TiZr	10	15	22	50	119	This work

FIGURE CAPTIONS

Figure 1. X-ray diffraction pattern of the NbCrMo_{0.5}Ta_{0.5}TiZr alloy in (a) as-solidified and (b) HIPd conditions. The indexed peaks belong to two BCC and one FCC crystal phases.

Figure 2. SEM backscatter electron images of a polished cross-section of the HIPd NbCrMo_{0.5}Ta_{0.5}TiZr alloy. The three phases with different morphologies and contrasts are indicated.

Figure 3. EBSD analysis of phases. (a) Secondary electron image, (b) phase map (BCC is red, FCC is green), and (c,d) inverse pole figure (IPF) maps of (c) the BCC phases and (d) the FCC phase. The crystallographic orientations of different grains in figures (c) and (d) are identified by the color scheme in the IPF triangle (e).

Figure 4. EDS maps of (a) Ti, (b) Ta and (c) Cr in different phases. The darker and lighter regions correspond to, respectively, lower and higher concentrations of the respective elements.

Figure 5. The dependence of the mass gain per the initial surface area of a NbCrMo_{0.5}Ta_{0.5}TiZr alloy sample on the oxidation time during oxidation in continuously flowing dry air at 1273 K.

Figure 6. A NbCrMo_{0.5}Ta_{0.5}TiZr alloy sample after oxidation in dry air at 1273 K for 100 hours. During cooling from 1273 K, six pieces of the oxide layer, corresponding to 6 faces of the sample, separated from the remaining sample core. The core piece is shown in the middle of the top row.

Figure 7. X-ray diffraction pattern of the oxide layer formed on the surface of the NbCrMo_{0.5}Ta_{0.5}TiZr alloy sample during holding at 1000°C for 100 hours. Complex oxides are detected.

Figure 8. Backscatter electron (BSE) image of a cross-section of the core (“non-oxidized”) piece (squared shape) and a separated oxide layer of a NbCrMo_{0.5}Ta_{0.5}TiZr alloy sample after oxidation in air for 100 hours at 1273 K. The cross-section of only one oxide plate (on the top) separated from the sample during cooling after oxidation is shown in this figure. Oxygen concentration profile was measured along the shown white horizontal line.

Figure 9. Microstructure of the oxide layer. BSE images taken at different magnifications.

Figure 10. (a) BSE and (b) SE images of the former BCC1 particle after oxidation.

Figure 11. (a) SE and (b) BSE images of the under-surface transition region of the core part of the oxidized sample.

Figure 12. A BSE image of the transition (partially oxidized) region of the core part. Areas and their ID numbers are shown, from which chemical compositions were determined. The compositions of these areas are given in Table 5.

Figure 13. Microstructure of a non-oxidized core part after holding for 100 h at 1273°K.

Figure 14.. Oxygen distribution (solid dark line) inside the core part along the horizontal line shown in Figure 8. The dashed vertical line corresponds to the sample surface. The blue dashed line is the oxygen diffusion model described by a sum of two Gaussian distributions (red and brown dotted lines).

Figure 15. The logarithmic dependence of the mass gain per the initial surface area of the NbCrMo_{0.5}Ta_{0.5}TiZr alloy sample on the time of oxidation in dry air at 1273 K. Dashed trendlines correspond to equations shown in the figure.

REFERENCES

- 1 D.M. Dimiduk and J.H. Perepezko, MRS Bulletin, 28 (2003) 639-645.
- 2 R.A. MacKay, T.P. Gabb, J.L. Smialek, and M.V. Nathal, Alloy Design Challenge: Development of Low Density Superalloys for Turbine Blade Applications, NASA/TM—2009-215819.
- 3 P.R. Subramanian, M.G. Mendiratta, D.M. Dimiduk, M.A. Stucke, Mater. Sci. Eng. A2390240 (1997) 1-13.
- 4 B.P. Bewlay, M.R. Jackson, J.-C. Zhao, and P.R. Subramanian, Metall. Mater. Trans. A 34A (2003) 2043-2052.
- 5 J.H. Perepezko, Science, 326, No. 5956 (2009) 1068-1069.
- 6 O.N. Senkov, G.B. Wilks, D.B. Miracle, C.P. Chuang, P.K. Liaw, Intermetallics, 18 (2010) 1758-1765.
- 7 O.N. Senkov, G.B. Wilks, J.M. Scott, D.B. Miracle, Intermetallics, 19 (2011) 698-706.
- 8 O.N. Senkov, J.M. Scott, S.V. Senkova, D.B. Miracle, C.F. Woodward, J. Alloys Comp. 509 (2011) 6043-6048.
- 9 O.N. Senkov, J.M. Scott, S.V. Senkova, D.B. Miracle, C.F. Woodward, J. Mater. Sci. (2012) DOI 10.1007/s10853-012-6260-2.
- 10 O.N. Senkov and C.F. Woodward, Mater. Sci. Eng. A 529 (2011) 311– 320.
- 11 J.-W. Yeh, S.-K. Chen, S.-J. Lin, J.-Y. Gan, T.-S. Chin, T.-T. Shun, C.-H. Tsau, S.-Y. Chang, Adv. Eng. Mater. 6 (5) (2004) 299–303.
- 12 J.-W. Yeh, Annales de Chimie: Science des Materiaux, 31 (2006) 633-648.
- 13 J.-W. Yeh, Y.-L. Chen, S.-J. Lin, S.-K. Chen, Mater. Sci. Forum, 560 (2007) 1-9.
- 14 R.A. Perkins, K.T. Chiang, G.H. Meier, Scripta Metall, 22 (1988) 419-424.
- 15 P.R. Subramanian, M.G. Mendiratta, D.M. Dimiduk, M.A. Stuke, Mater. Sci. Engr. A239-240 (1997) 1-13.

-
- 16 N. Birks and G.H. Meier: *Introduction to High Temperature Oxidation of Metals*, (Edward Arnold (Publishers) Ltd. London, England, 1983).
- 17 O. Kubaschewski and B.E. Hopkins: *Oxidation of Metals and Alloys. 2nd edition*, (Butterworth and Co. Ltd., London, England, 1962).
- 18 J.M. West: *Basic Corrosion and Oxidation*, (Ellis Horwood Limited, Market Cross House, Cooper Street, Chichester, West Sussex, PO19 1EB, England, 1980).
- 19 H.L. Bernstein: Metall. Trans. A. 18A (1987) 975-985.
- 20 J.J. Harwood, Materials and Methods, 44 (6) (1956) 84-89.
- 21 M.G. Mendiratta, T.A. Parthasarathy, D.M. Dimiduk, Intermetallics, 10 (2002) 225-232.
- 22 M. Meyer, M. Kramer and M. Akinc, Adv. Materials, 8 (1) (1996) 85-88.
- 23 R.A. Perkins and G.H. Meier, JOM 42 (8) (1990) 17-21.
- 24 M.R. Jackson, B.P. Bewlay, R.G. Rowe, D.W. Skelly, H.A. Lipsitt, JOM 48 (1) (1996) 39-44.
- 25 D. Yao, C. Zhou, J. Yang, H. Chen, Corrosion Science, 51 (2009) 2619-2627.
- 26 P.R. Subramanian, M.G. Mendiratta, D.M. Dimiduk, M.A. Stucke, Mater. Sci. Eng. A239-240 (1997) 1-13.
- 27 E.S.K. Menon, M.G. Mendiratta, D.M. Demiduk, Structural Intermetallics 2001, K.J. Hemker, D.M. Dimiduk, H. Clemens, R. Darolia, H. Inui, J.M. Larsen, V.K. Sikka, M. Thomas, J.D. Whittenberger (Eds.) TMS, Materials Park, OH, 2001, pp. 591-600.
- 28 Y. Murayama, S. Hanada, Sci. tech. Adv. Mater. 2 (2002) 145-156.
- 29 K. Chattopadhyay, R. Mitra, K.K. Ray, Metall. Mater. Trans. A 39A (2008) 577-592.
- 30 R.A. Perkins, R.A. Padgett, Jr. Acta Metall. 25 (1977) 1221-1230.
- 31 R.J. Farraro, R.B. McLellan, Mater. Sci. Eng. 33 (1978) 113-116.

Figures

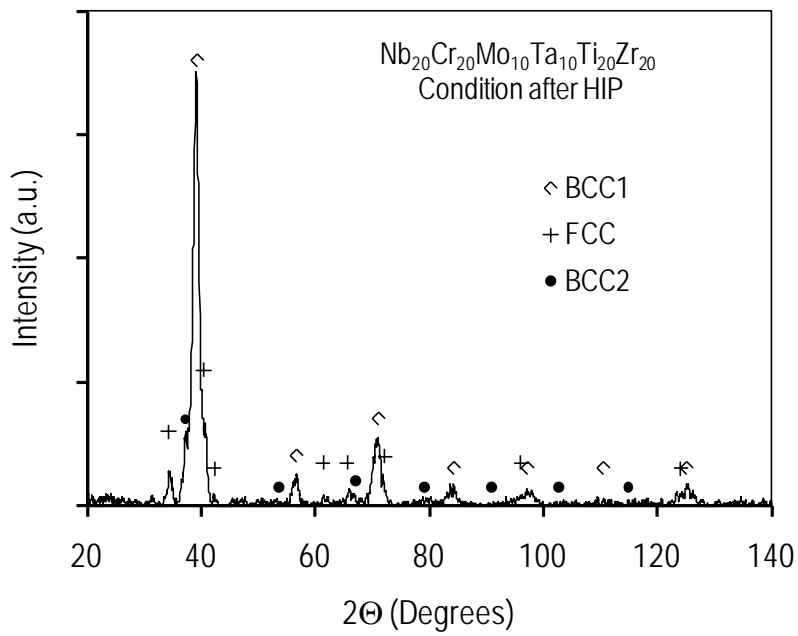


Figure 1. X-ray diffraction patterns of the $\text{NbCrMo}_{0.5}\text{Ta}_{0.5}\text{TiZr}$ alloy after HIPing at 1723 K for 3 hours.

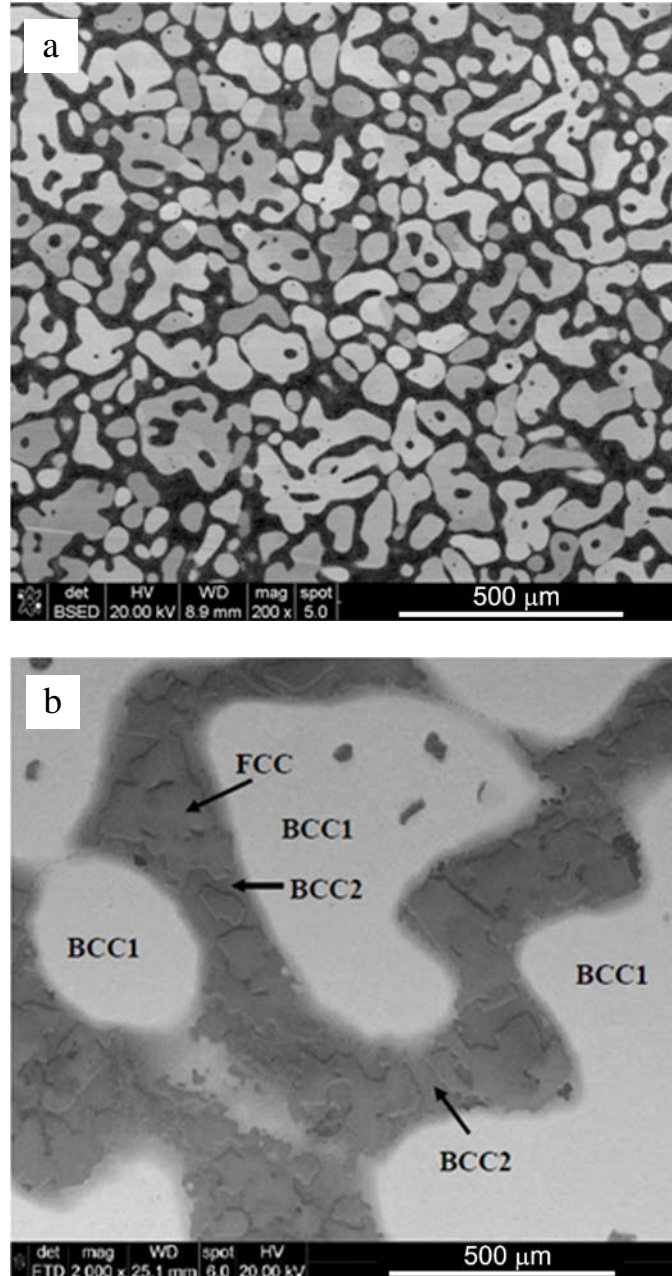


Figure 2. SEM backscatter electron images of a polished cross-section of the NbCrMo_{0.5}Ta_{0.5}TiZr alloy. (a) A low magnification image showing the duplex structure; (b) A high magnification image illustrating three phases, which have different morphologies and electron backscatter contrasts.

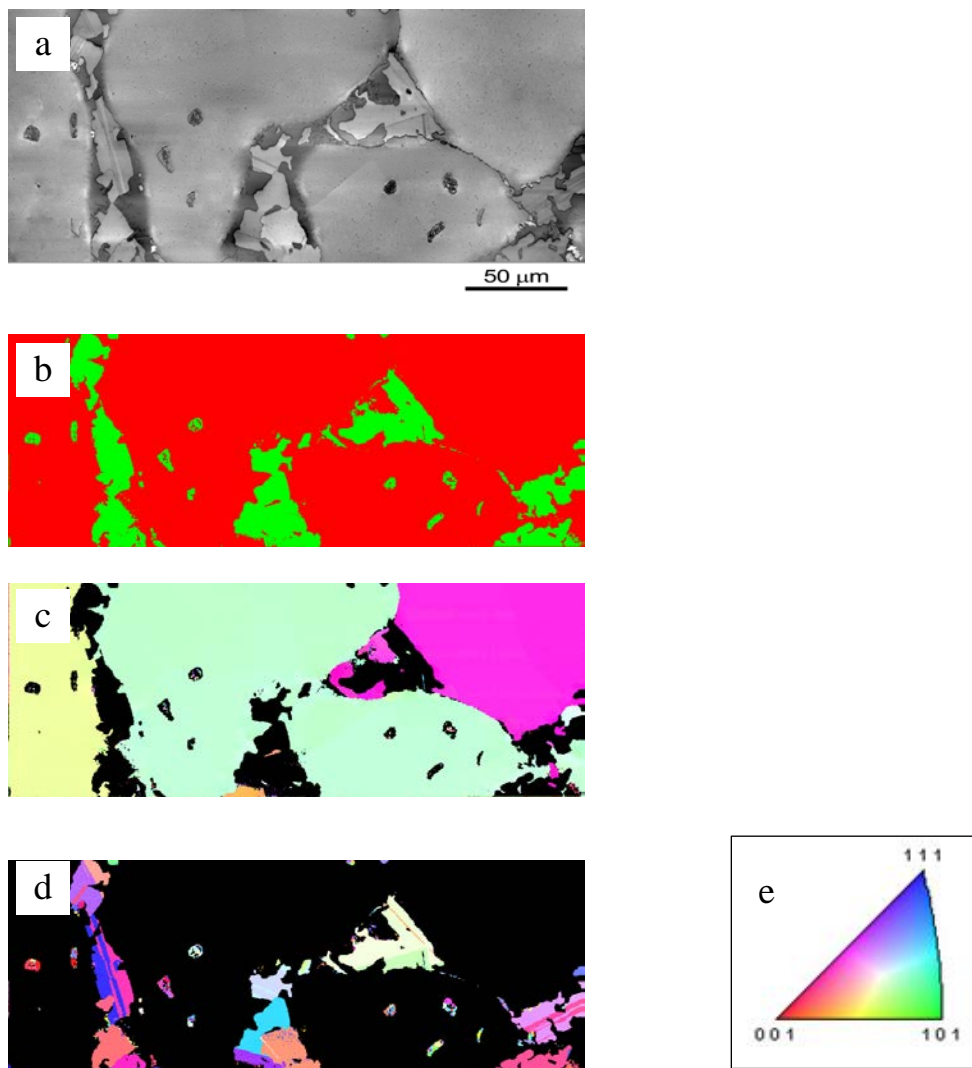


Figure 3. EBSD analysis of phases. (a) Secondary electron image, (b) phase map (BCC is red, FCC is green), and (c,d) inverse pole figure (IPF) maps of (c) the BCC phases and (d) the FCC phase. The crystallographic orientations of different grains in figures (c) and (d) are identified by the color scheme in the IPF triangle (e).

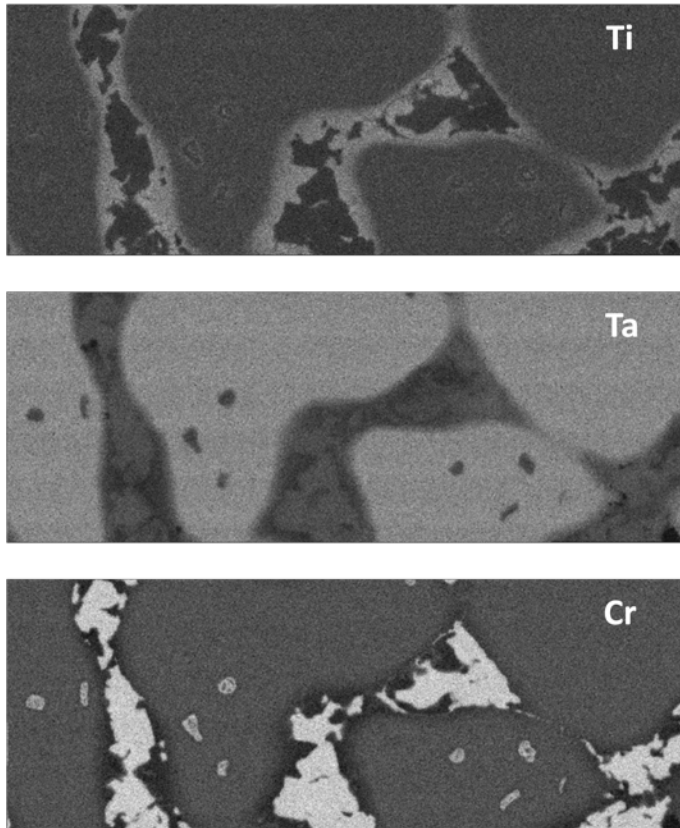


Figure 4. EDS maps of (a) Ti, (b) Ta and (c) Cr in different phases. The darker regions correspond to a smaller and lighter regions correspond to a higher concentration of the respective element.

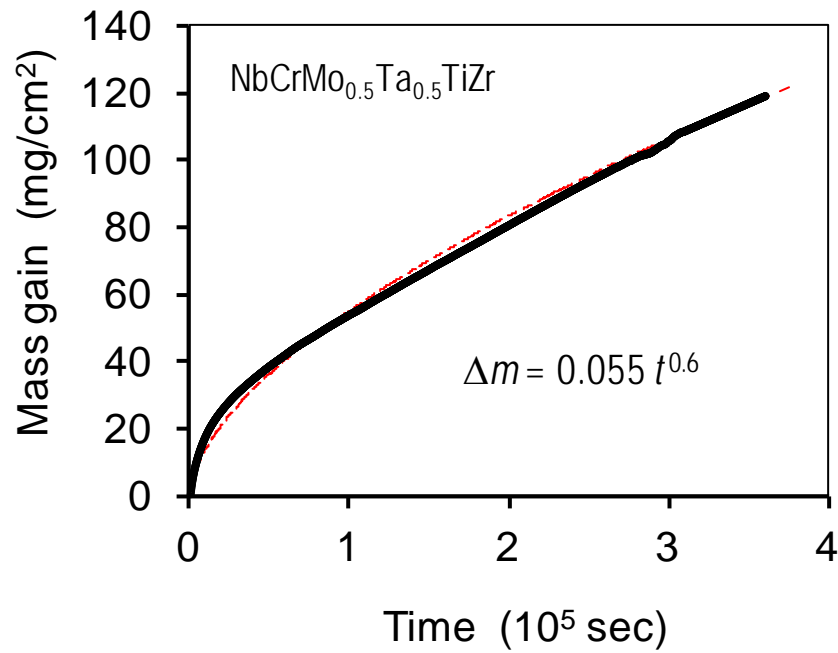


Figure 5. The dependence of the mass gain per the initial surface area of a NbCrMo_{0.5}Ta_{0.5}TiZr alloy sample on the oxidation time during oxidation in continuously flowing dry air at 1273 K. The red dashed trendline follows the equation shown in the figure.

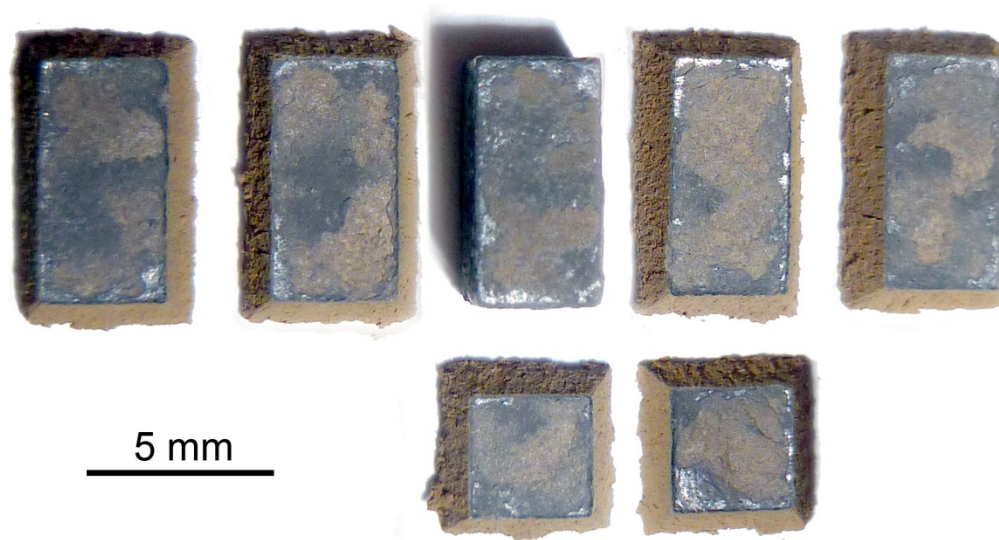


Figure 6. A NbCrMo_{0.5}Ta_{0.5}TiZr alloy sample after oxidation in dry air at 1273 K for 100 hours. During cooling from 1273 K, six pieces of the oxide layer, corresponding to 6 faces of the sample, separated from the remaining sample core. The core piece is shown in the middle of the top row.

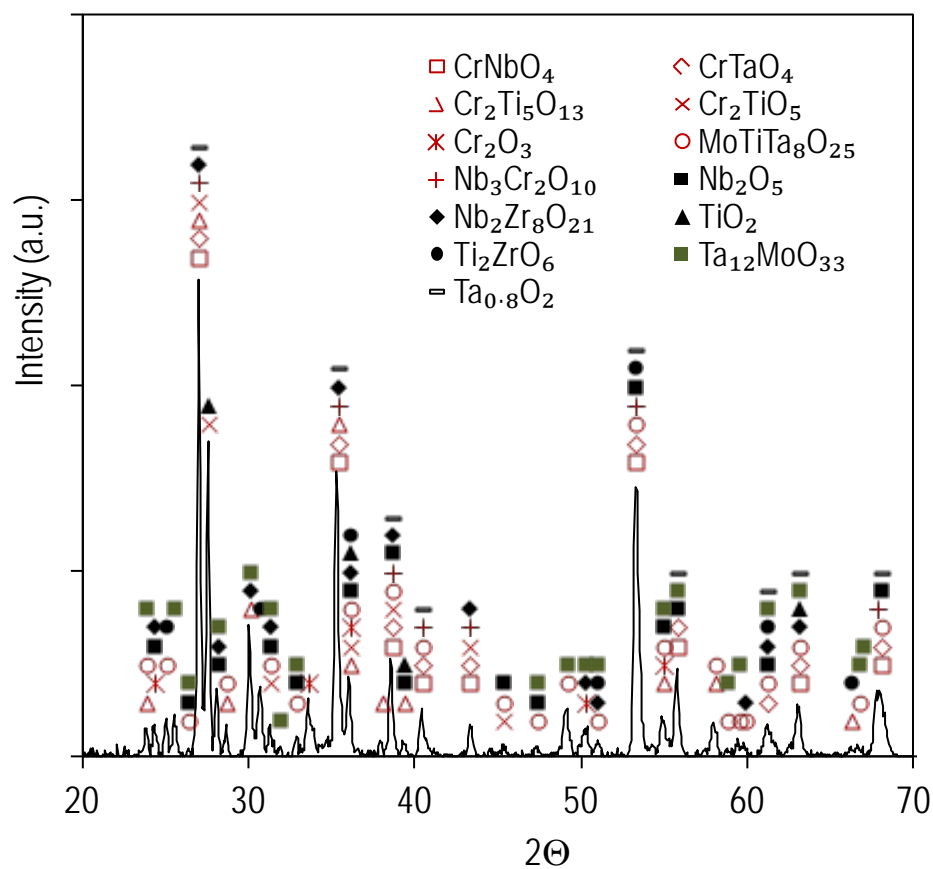


Figure 7. X-ray diffraction pattern of the oxide layer formed on the surface of the NbCrMo_{0.5}Ta_{0.5}TiZr alloy sample during holding at 1000°C for 100 hours. Complex oxides are detected.

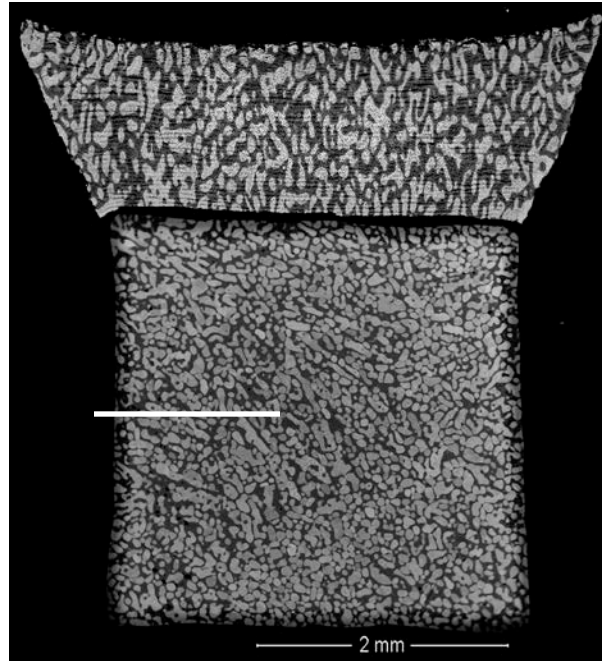


Figure 8. Backscatter electron (BSE) image of a cross-section of the core (“non-oxidized”) piece (squared shape) and a separated oxide layer of a $\text{NbCrMo}_{0.5}\text{Ta}_{0.5}\text{TiZr}$ alloy sample after oxidation in air for 100 hours at 1273 K. The cross-section of only one oxide plate (on the top) separated from the sample during cooling after oxidation is shown in this figure. Oxygen concentration profile was measured along the shown white horizontal line.

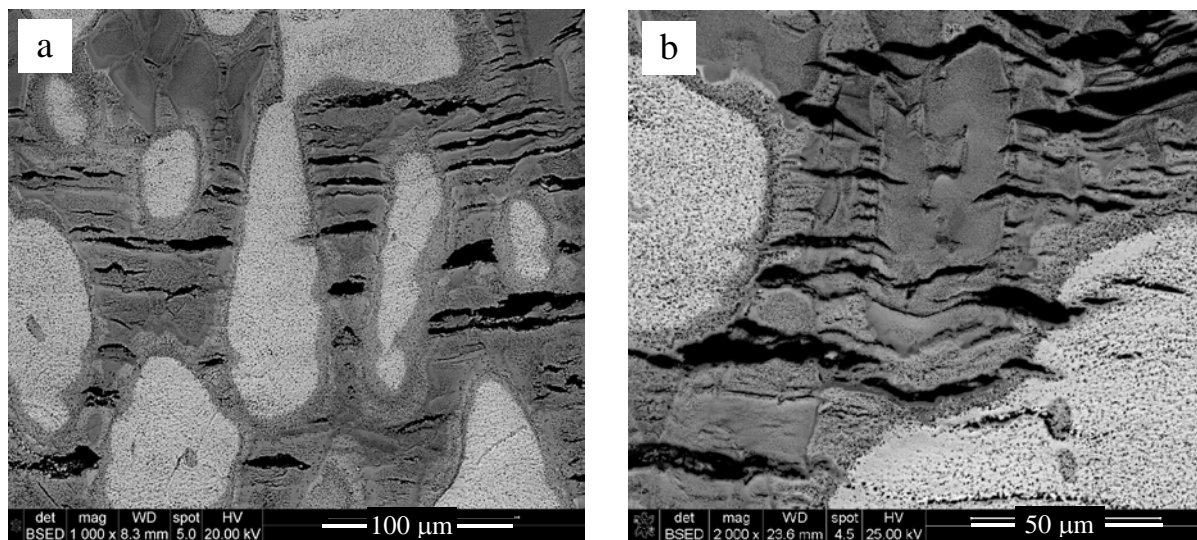


Figure 9. Microstructure of the oxide layer. BSE images taken at different magnifications.

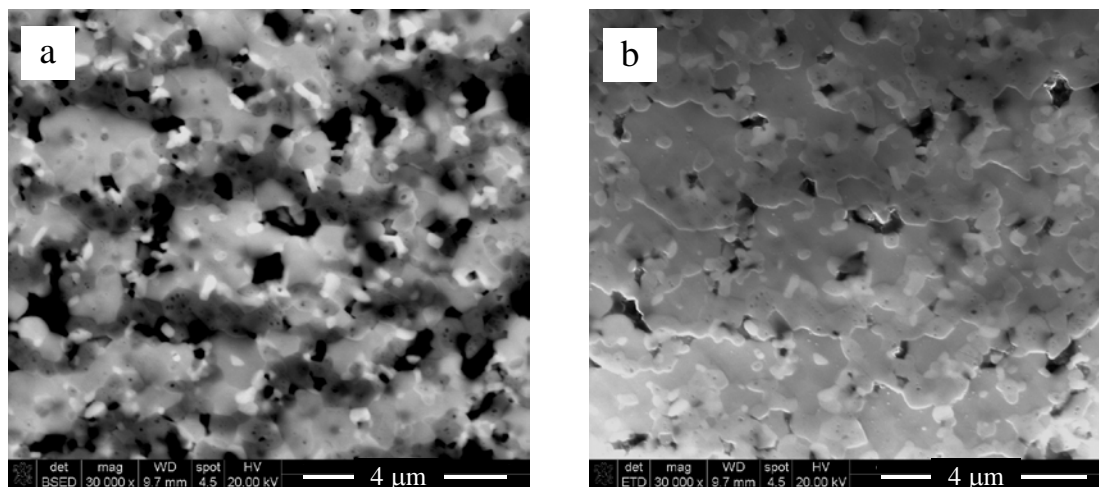


Figure 10. (a) BSE and (b) SE images of the former BCC1 particle after oxidation.

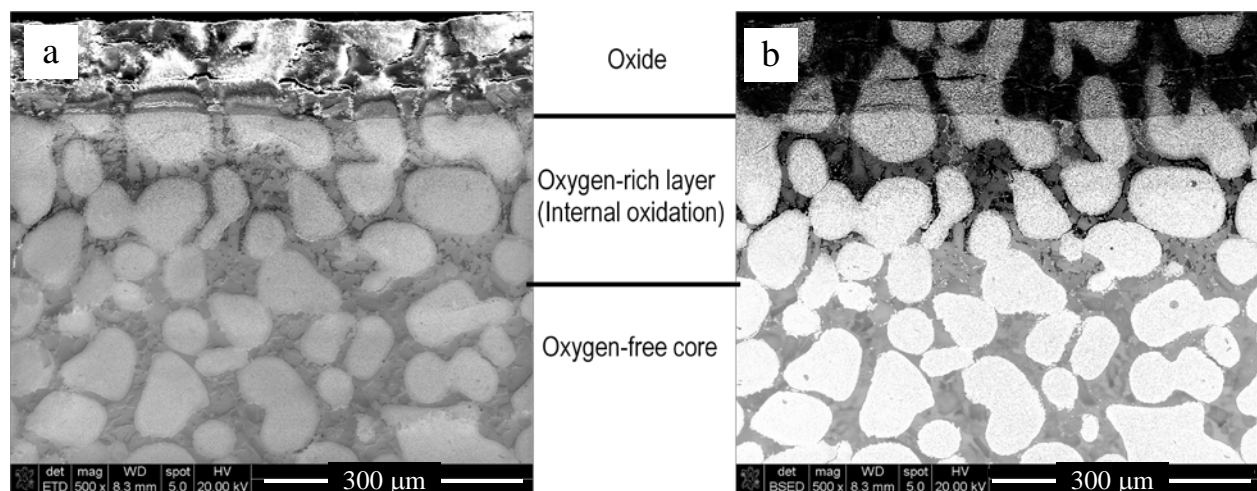


Figure 11. (a) SE and (b) BSE images of the under-surface transition region of the core part of the oxidized sample.

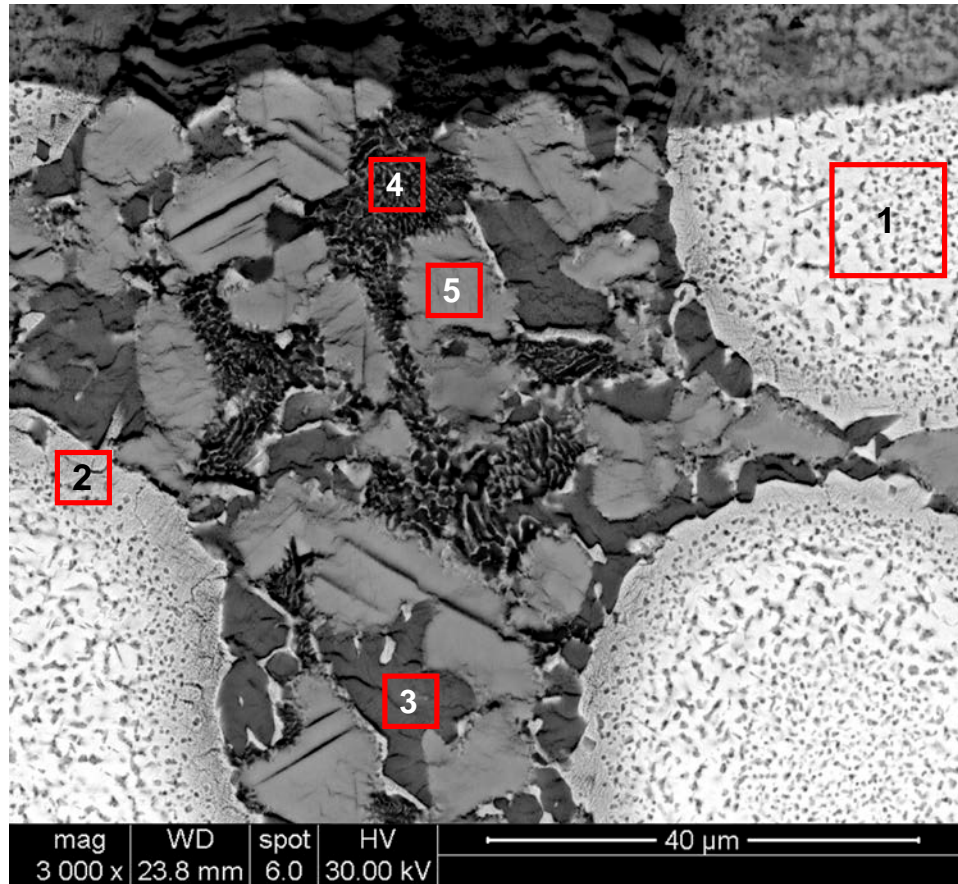


Figure 12. A BSE image of the transition (partially oxidized) region of the core part. Areas are shown, from which chemical compositions were determined.

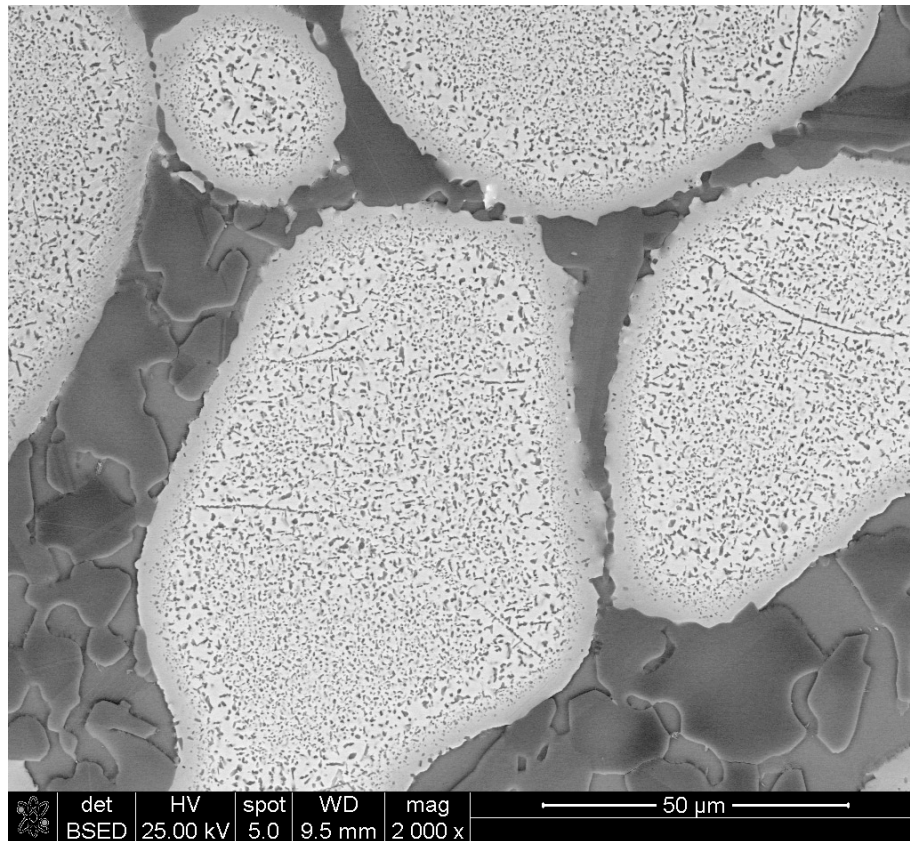


Figure 13. Microstructure of a non-oxidized core part after holding for 100 h at 1273°K.

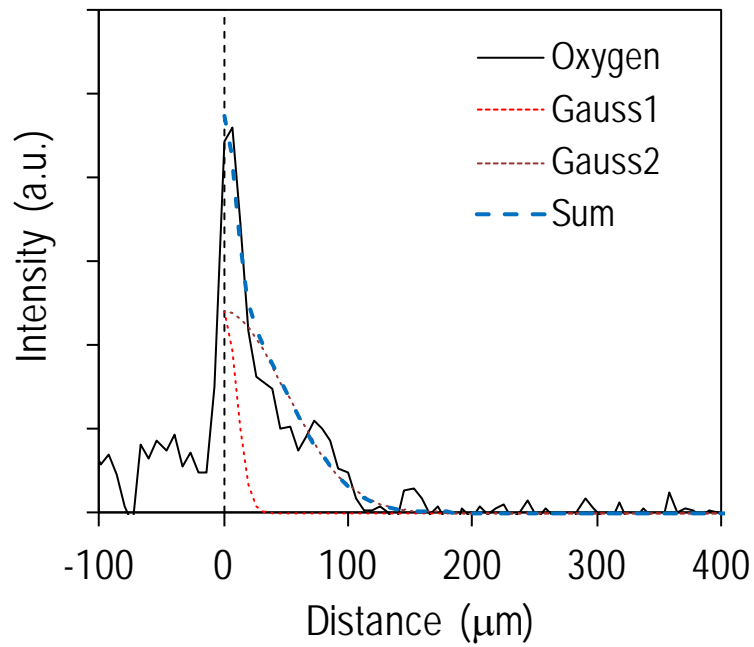


Figure 14. The oxygen concentration profile (solid dark line) inside the core part along the horizontal line shown in Figure 8. The dashed vertical line corresponds to the oxide/core matrix interface. The profile can be described as a sum of two Gaussian distributions, $C = A \exp[-(x/\sigma)^2/2]$, where x is the distance from the interface and σ is the standard deviation. For the first Gaussian (Gauss1), $\sigma_1 = 10 \mu\text{m}$, and for the second Gaussian (Gauss2), $\sigma_2 = 50 \mu\text{m}$.

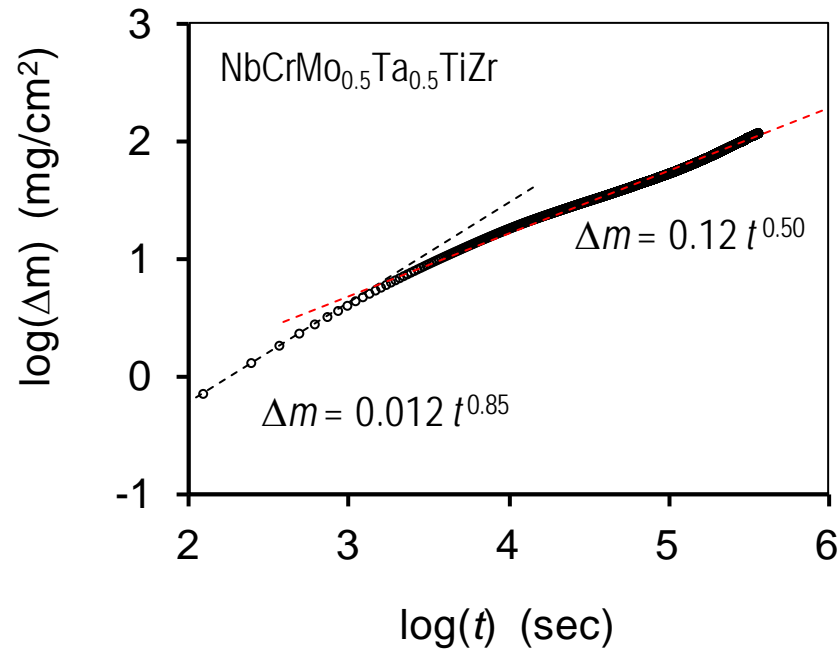


Figure 15. The logarithmic dependence of the mass gain per unit surface area of the NbCrMo_{0.5}Ta_{0.5}TiZr alloy sample on the time of oxidation in dry air at 1273 K. Dashed trendlines correspond to equations shown in the figure.